Monopile-mounted Wave Energy Converter for a Hybrid Wind-Wave System

C. Perez-Collazo[AB*], R. Pemberton[B], D. Greaves[B] G. Iglesias[BC],

[A] School of Mines and Energy Engineering, University of Vigo, R./ Maxwell s/n. Vigo, Spain

[B] School of Engineering, University of Plymouth, Reynolds Building, Plymouth, PL4 8AA, UK

[C] MaREI, Environmental Research Institute & School of Engineering, University College Cork, Ireland

[*] Corresponding author

Email: carlos.perez.collazo@uvigo.es

Abstract:

Multipurpose platforms are innovative solutions to combine the sustainable exploitation of multiple marine resources. Among them, hybrid wind-wave systems stand out due to the multiple synergies between these two forms of marine renewable energy. The objective of this work is to develop a hybrid system for monopile substructures, which are currently the prevailing type of substructure for offshore wind turbines, and more specifically to focus on the wave energy converter sub-system, which consists in an oscillating water column. For this purpose, an in-depth experimental campaign was carried out using a 1:40 scale model of the wave energy converter sub-system and the monopile substructure, considering regular and irregular waves. Based on the experimental results the performance of the device and its interaction with the wave field were characterised – a fundamental step to fully understand the benefits and limitations of this hybrid wind-wave system, which sets the basis for its future development. Regarding the performance, the best efficiency was obtained with the turbine damping corresponding to a 0.5% orifice size, and two resonance peaks were identified (T = 9 and 6 s). As for the interaction of the hybrid system with the wave field, between 5% and 66% of the incident wave power is reflected and between 3% and 45%, transmitted. The wave period was found to be the parameter that most influenced wave run-up on the substructure. This characterisation of the behaviour of the hybrid system shows that it is indeed a promising option for further development.

Keywords: Hybrid wind-wave; Wave energy, Offshore Wind; OWC; Physical modelling

Highlights:

- A hybrid wind-wave energy converter for monopile substructures is developed
- A thorough experimental campaign is carried out using a 1:40 model
- The interaction of the hybrid energy converter with the wave field is characterised
- The influence of turbine damping and wave conditions on performance is assessed

1. Introduction

In the current scenario of climate change[1], with the marine environment under threat [2], a rapid transition towards a sustainable and environmentally-friendly economy is a pressing challenge that our society cannot afford to postpone [3], . In this transition offshore renewable energy (ORE) technologies are poised to play a leading role. With 18.8 GW of installed capacity worldwide at the end of 2017 [4], of which 15.8 GW in Europe [5], the European offshore wind sector is clearly leading the transition towards a sustainable energy system. This exceptional development has raised great expectations and pushed the industry to set the target of installing 460 GW of offshore wind energy, in European waters, by 2050 [6]. To realise this target and to make the offshore wind industry become the large-scale clean energy provider that it is expected to, the present momentum in the sector must be strengthened.

To increase the sustainability of offshore wind installations, at a time when they are becoming more and more popular in many regions worldwide, multipurpose platforms arise as an alternative to conventional offshore wind systems [7], which enables other resources in the same marine space to be exploited in addition to wind energy itself [8] – wave energy [9], maritime leisure [10], aquaculture and seaweed farming [11], fisheries, logistic nodes. In this manner, the use of marine space is optimised. Hybrid wind-wave energy systems are a particular type of multipurpose platforms that is predicated on the multiple synergies between offshore wind and wave energy installations, as described in [12], previously outlined in [13] and [14], and further investigated by [15].

Research on hybrid wind-wave systems has been driven primarily by a number of European research projects aimed at developing the concept of hybrid and multiplatform systems, and at setting the basis for a future involvement of European industry (e.g., Marina Platform[16], ORECCA [17], TROPOS [18], H2OCEAN [19] and MERMAID [20]). These projects set the basis with a series of incipient concepts, such as: Floating Power Plant [21], NEMOS [22], Wave Star [23] and W2Power [24]. However, the number of works addressing the development of hybrid wind-wave systems is rather limited. Zanuttigh et al. [25] present a methodology a multi-criteria design of multi-use offshore

63 platforms, O'Sullivan's PhD [26] addresses the feasibility of different combined wind-wave platforms
64 in the framework of the MARINA Platform project, further investigated in [27] and [28]. The
65 development of hybrid solutions for floating wind is further investigated in several works, e.g., [29].
66 The characterisation of the joint wind-wave resource has been investigated by [30] for islands and [31]
67 at a global level. The variability and predictability of the combined wind-wave resource has been
68 investigated by [32]. The potential co-location of both technologies was addressed in [33]. Other
69 publications have addressed the manner in which the temporal correlation of wind and wave resources
70 influences the combined power output (e.g., [34]) and its interaction with the electric grid (e.g., [35]),
71 as well as the potential of combined wind-wave systems to smooth the power output and reduce
72 downtime [36]. Finally, the interesting concept of the 'shadow-effect' [37], i.e., how wave energy
73 converters (WECs) deployed around the periphery of a wind farm can result in a milder wave climate
74 within the farm and thus reduce its operational costs was studied by [38].

75 This paper deals with the development through laboratory tests of the University of Plymouth's
76 hybrid wind-wave energy converter presented in [39] and further investigated for jacket-frame
77 substructures in [40], which integrates an oscillating water column (OWC) with an offshore wind
78 substructure of the monopile type (Figure 1). For this research, a 1:40 scale model, of an upgraded
79 version of the hybrid system considered in [41], was manufactured and tested. The wave climate of an
80 offshore wind farm off the west coast of Denmark was taken as a reference. Based on the experimental
81 results, the interaction of the hybrid system with the wave field was established.

82 This article is structured as follows. Section 2 describes the materials and methods used during
83 the experimental campaign. Results from the experimental campaign are presented in Section 3, and
84 discussed in Section 4. Finally, conclusions are drawn in Section 5.
85

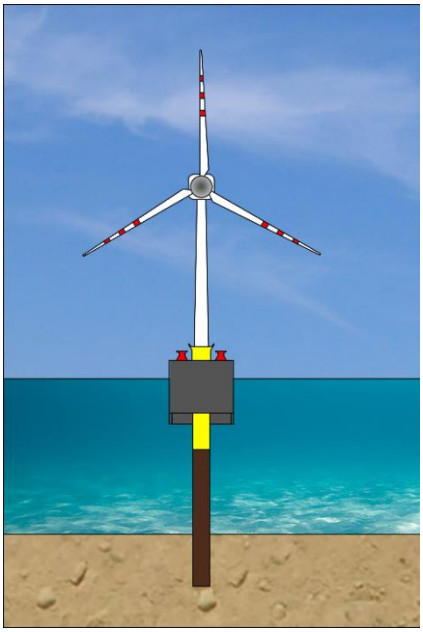

(**a**)

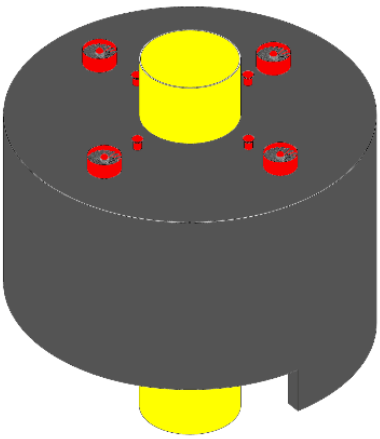

(**b**)

Figure 1: University of Plymouth's hybrid wind-wave energy converter: (a) conceptual representation of the hybrid system for monopile offshore wind substructures; and (b) perspective view of the WEC sub-system; (partially reproduced from [40])

2. Materials and methods

The materials and methods considered for the physical modelling campaign of the hybrid wind-wave energy converter can be structured into three different sections: (i) the definition of the physical model itself, (ii) the description of the experimental facility, set-up and test programme, and finally, (iii) the data analysis techniques followed to process the data obtained in the experimental campaign.

2.1. The hybrid model

A 1:40 scale model (Figure 2) was built based on the proposed hybrid device. The design of the model was carried out considering multiple factors, such as: experience from previous models, available 'out-of-the-shelf' materials for model manufacturing and the capabilities of the experimental facility, and the reference text [43]. Table 1 defines the most relevant dimensions of the model. The Froude similarity criterion was applied. The scale model was designed in accordance with: (i) the most common diameters of monopile substructures being installed in offshore windfarms; (ii) the dimensions of the wave basing where the tests are to be conducted; (iii) the sensitivity and working

ranges of the sensors; (iv) the water depth and wave conditions tested, and if these are within the working limits of the wave maker. Only the WEC sub-system was considered for this experimental campaign, as the wind turbine sub-system does not influence significantly its hydrodynamic response.

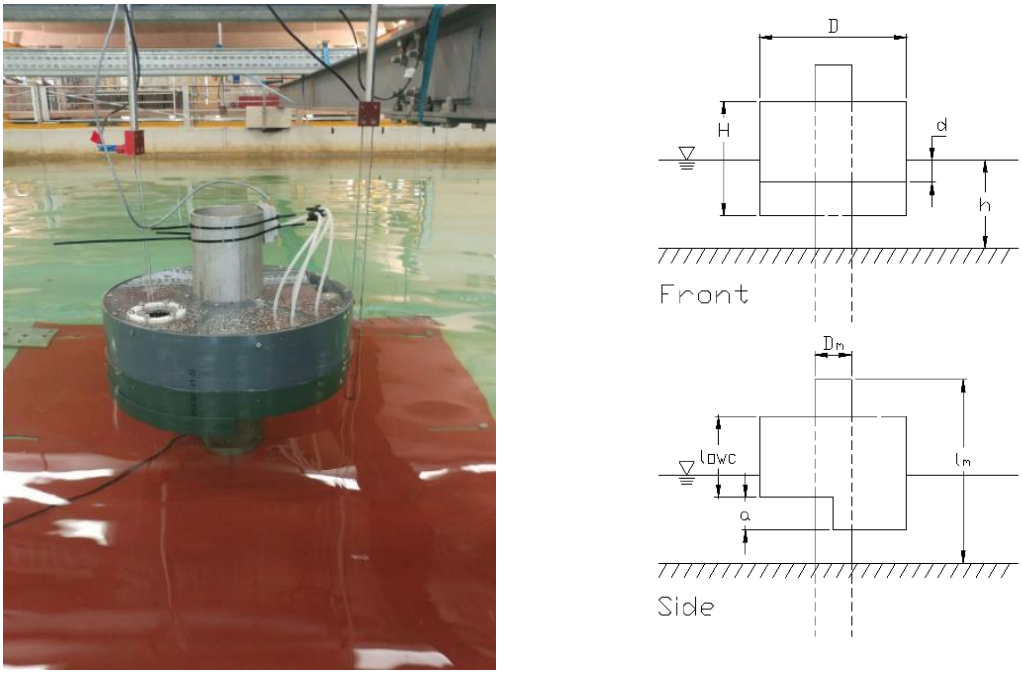

(**a**) (**b**)

Figure 2: 1:40 scale model of the hybrid device: (a) being tested at the University of Plymouth's COAST Laboratory and (b) a sketch showing front and side views of the model

Table 1: Model characteristics and dimensions

Parameter	Symbol	Dimension
Chamber draught	d	0.100 m
Chamber external diameter	D	0.500 m
Chamber height	l_{owc}	0.275 m
Chamber wall-thickness	e_c	4.0 x 10^{-3} m
Inner chamber water plane area	A_{owc}	0.174 m^2
Monopile external diameter	D_m	5.563" (0.141 m)
Monopile length	l_m	0.750 m
Monopile wall-thickness	e_m	0.258" (6.6 x 10^{-3} m)
Skirt length	a	7.5 x 10^{-2} m
Skirt angle	α	180 deg
Water depth	h	0.500 m

The model of the hybrid device was built considering materials, such as: PVC, methacrylate, stainless steel and mild steel. A 500 mm external diameter PVC pipe with a wall thickness of 4 mm was used to build the OWC chamber. The skirt section was built out of an angular section of the same PVC pipe as the OWC chamber. Two internal radial reinforcement beams were laser cut out of a 10 mm thickness PVC sheet. The OWC chamber's lid was built out of a 10 mm thickness methacrylate sheet. A 5" internal diameter stainless steel pipe (manufacturing schedule 40) was used to build the offshore wind turbine monopile. Two annular rings, built out of a 6 mm thickness stainless steel plate, were welded to the monopile as attachment points for the OWC chamber. A 6 mm thickness stainless steel disk was welded at the bottom part of the monopile to solidary link the model to a square, 6 mm thickness, mild-steel plate, as the main support of the model, which was screwed to the bottom of the basin. The damping induced by the full-scale power take-off (PTO) on the WEC sub-system – i.e., an impulse turbine – was modelled by means of a number of exchangeable perforated plates with different orifice diameters, a common technique followed by numerous authors (e.g., [44]). The values of the orifice diameter selected (34 mm, 42 mm, 48 mm and 60 mm) corresponded to the following values of the area coefficient [45]: 0.5%, 0.75%, 1% and 1.5%, respectively.

2.2. Experimental set-up and test programme

The University of Plymouth's COAST Laboratory, and in particular its coastal basin, was the facility used for the experimental campaign. This is a 15 m long and 10 m wide wave basin, with a variable water depth of up to 500 mm. For this work the water depth was set at 500 mm to match the 20 m water depth of the Horns Rev 3 offshore wind farm, off NW Denmark. In particular, the MetOcean study for this offshore wind farm [46] was used as a reference for selecting a realistic set of wave conditions for a monopile based offshore wind farm (Figure 3). A wave-maker, from Edinburgh designs ltd (EDL), is used to generate the waves. In relation to the tide, the power extraction of a fixed OWC has been proved to be affected by the variation of the tidal level for fixed OWC systems (e.g.,

[47]). This has not been considered in this work, for the hybrid system considered here has the capability to adapt to the tidal level by raising or lowering the OWC, as described in the patent [48].

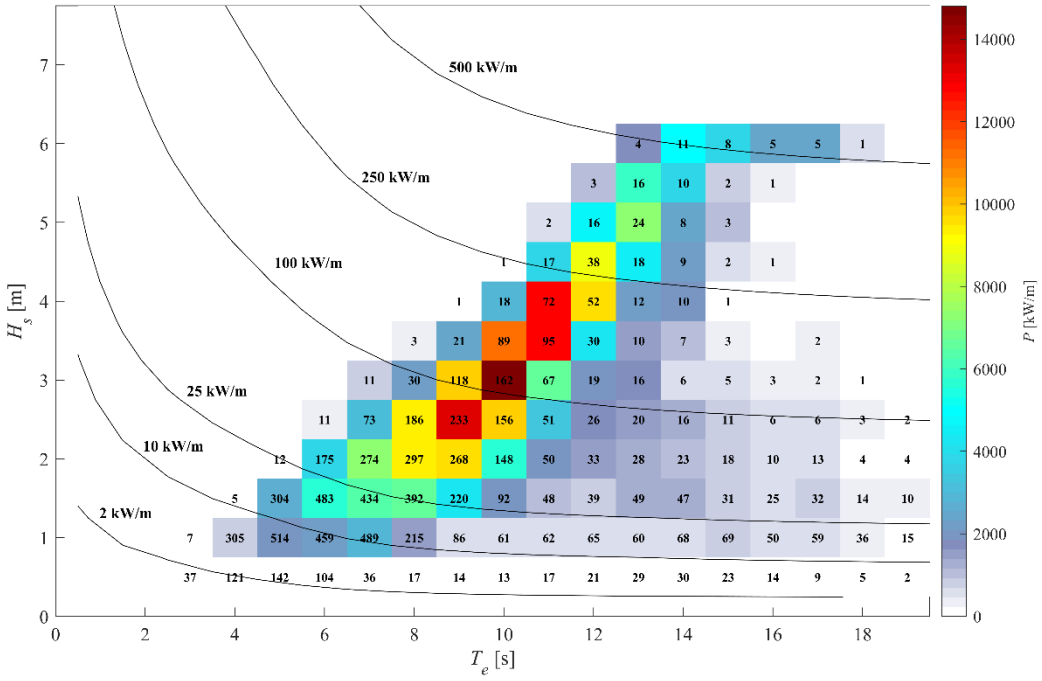

Figure 3: Horns Rev 3 significant wave height – energy period scatter diagram. The curves represent wave power isolines, and the numbers, hours in an average year of the corresponding *energy bin*

For the experimental set-up (Figure 4), six conductive wave gauges were positioned along the basin to record free surface elevation. The first three wave gauges (WG1, WG2 and WG3), in front of the model, were used to record the input signals for incident and reflected wave analysis (IRWA), following the Mansard and Funke [49] wave reflection analysis method as modified by Baquerizo et al. [50]. Another wave gauge (WG4) was used to record the wave run-up at the front of the model and positioned at the front of the model – in contact with the OWC chamber external surface. WG6 was installed in the OWC chamber to record free surface motion. Finally, WG5 was installed in the lee of the model to record the transmitted wave. Furthermore, an Omega differential pressure transducer (PT), PX2650-10BD5V, was set up to measure the pressure inside the OWC chamber with reference to the outer (atmospheric) pressure. Table 2 defines the position, along the centreline of the basin, of

150 the different elements of the experimental set-up – the coordinate system for the experiments follows
151 the convention defined in [41].

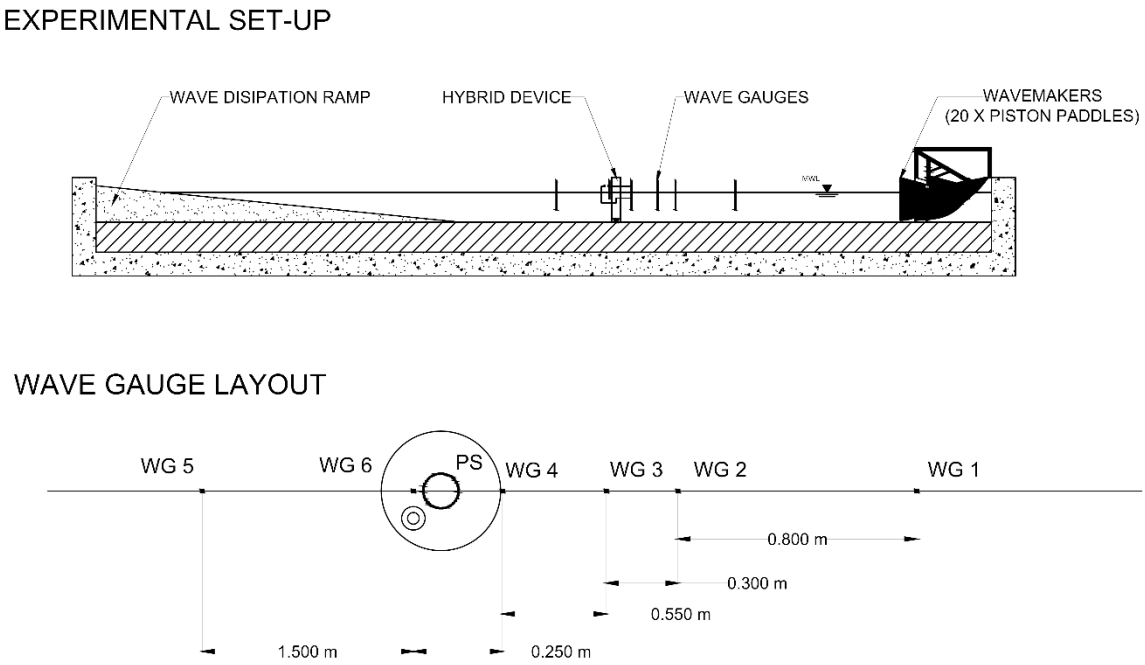

152

153 **Figure 4:** Lateral view of the flume and schematic of the wave gauge layout

154

155 **Table 2:** Position of wave gauges and model

Element	X [m]
WG1	2.475
WG2	3.275
WG3	3.575
WG4	4.125
Hybrid device model	4.375
Pressure transducer (PT)	4.375
WG5	5.875
WG6 (OWC)	4.375

156

157 Regular and irregular waves, together with four different orifice sizes, were considered to define the
158 experimental programme –the 48 mm orifice size (1%) alone was used in the tests with irregular waves.
159 The experimental campaign was structured into four different experimental series, following [43].
160 Series A defines the regular waves tests, while Series B and C does it for the irregular waves tests.

Finally, Series R covers the repeatability tests for both regular and irregular waves. Table 3 defines the wave conditions matrix for Series A, where the duration for each one of the regular waves tests was set to 100 times the wave period. Furthermore, Table 4, shows the irregular sea states – considering a JONSWAP spectrum [47] – for Series B and C, where the duration of the tests was set at a minimum of 569 s – i.e., 60 min at prototype scale.

Table 3: Wave conditions for Series A, regular waves (data in prototype values)

Series A		**T [s]**									
		4	*5*	*6*	*7*	*8*	*9*	*10*	*11*	*12*	*13*
H [m]	*1.5*	A01	A02	A04	A06	A09	A13	A18	A23	A28	A33
	2.5		A03	A05	A07	A10	A14	A19	A24	A29	A34
	3.5				A08	A11	A15	A20	A25	A30	A35
	4.5					A12	A16	A21	A26	A31	A36
	5.5						A17	A22	A27	A32	A37

Table 4: Wave conditions for Series B and C, irregular waves (data in prototype values)

Test Series	**Test number**	**H_S**	**T_E**	**T_Z**	**T_P**
Series B	B01	1.5 m	5.13 s	4.28 s	5.50 s
	B02	1.5 m	6.07 s	5.06 s	6.50 s
	B03	2.5 m	7.00 s	5.83 s	7.50 s
	B04	2.5 m	7.93 s	6.61 s	8.50 s
	B05	3.5 m	8.86 s	7.39 s	9.50 s
	B06	3.5 m	9.80 s	8.16 s	10.50 s
	B07	4.5 m	9.80 s	8.16 s	10.50 s
	B08	4.5 m	10.73 s	8.94 s	11.50 s
Series C	C01	1.5 m	4.20 s	3.50 s	4.50 s
	C02		5.13 s	4.28 s	5.50 s
	C03		6.07 s	5.06 s	6.50 s
	C04		7.00 s	5.83 s	7.50 s
	C05		7.93 s	6.61 s	8.50 s
	C06		8.86 s	7.39 s	9.50 s
	C07		9.80 s	8.16 s	10.50 s
	C08		10.73 s	8.94 s	11.50 s
	C09		11.66 s	9.72 s	12.50 s
	C10		12.60 s	10.50 s	13.50 s

The accuracy of the experimental set-up was evaluated through the repeatability tests (Series R), which was divided into two subseries: Series RA for regular waves, and RB for random waves. For regular waves four different wave conditions were selected (A06, A08, A18, and A20 from Table 3), while,

for irregular waves two were the sea states selected (B04 and B05, from Table 4). Four consecutive tests were run for each one of the wave conditions defined for each subseries. Based on the recorded data, the repeatability of the experimental campaign was assured, as may be observed from the values of the statistical indicators in Table 5 – the correlation coefficient (R^2) and the normalised root mean square error (*NRMSE*) (Appendix A).

Table 5: Average values of R^2 (correlation coeff.) and *NRMSE* (normalised root-mean-square error) for the repeatability tests series

		WG1	WG2	WG3	WG4	WG5	WG6	PT
Series RA	R^2	0.991	0.983	0.987	0.984	0.977	0.978	0.992
	NRMSE	5.66%	7.06%	6.34%	6.99%	8.59%	8.48%	4.76%
Series RB	R^2	0.970	0.958	0.958	0.934	0.951	0.951	0.992
	NRMSE	4.15%	5.31%	4.80%	4.95%	5.67%	6.11%	1.90%

2.3. Data analysis

The interaction of the hybrid wind-wave energy converter with the wave field may be characterised based on the reflection (K_R) and transmission (K_T) coefficients. For its part, the performance of the system may be assessed using the response amplitude operators for the following: (i) free surface oscillation within the OWC chamber (RAO_C); (ii) relative pressure in the chamber (RAO_P); (iii) run-up coefficient, in different versions for regular (C_R) and random (C_S *and* C_{max}) waves; and (iv) the capture-width ratio (C_{WR}). In the case of regular waves:

$$K_R = \frac{H_R}{H_I}, \tag{1}$$

$$K_T = \frac{H_T}{H_I}, \tag{2}$$

$$C_{WR} = \frac{P_m}{P\ b}. \tag{3}$$

$$RAO_C = \frac{H_C}{H_I}, \tag{4}$$

$$RAO_P = \frac{1}{\rho_w g}\frac{H_P}{H_I}, \tag{5}$$

$$C_R = \frac{R}{H_I}, \tag{6}$$

In the foregoing equations P denotes wave power per metre of wave front; P_m represents the average pneumatic power captured by the system, b represents the width of the OWC device – in this case, the external diameter of the OWC chamber (D); H_C is defined as the range of the free surface oscillation, and H_P as the range of the pneumatic pressure, within the same oscillation cycle; R stands for wave run-up in front of the model; H_I, H_R and H_T stand for the incident, reflected and transmitted wave height, respectively; g stands for the acceleration of gravity; ρ_w represents the density of water.

$$P = \frac{\rho_W g H_I^2 c_g}{8}, \tag{7}$$

$$P = \rho_W g \sum_{i=1}^{N} S_i(c_g)_i \Delta f \tag{8}$$

where N is the number of frequency components or bands (for each Δf), and Si and $(c_g)_i$ are the spectral density and the group velocity for the i-th band, respectively.

Alternatively, for irregular waves:

$$K_R = \sqrt{\frac{m_{0R}}{m_{0I}}}, \tag{9}$$

$$K_T = \sqrt{\frac{m_{0T}}{m_{0I}}}, \tag{10}$$

$$C_S = \frac{R_S}{H_{SI}}, \tag{11}$$

$$C_{max} = \frac{R_{max}}{H_{SI}}, \tag{12}$$

where m_{0I}, m_{0R} and m_{0T} are the zero-th order moment of the incident, reflected and transmitted waves, respectively. R_S and R_{max} are the significant and maximum wave run-up respectively, with H_{SI} the incident significant wave height. Note that the capture-width ratio (C_{WR}), defined from Equation 3, is valid for both, regular and irregular waves. Further details about this method and the definition of some of the parameters can be found in [40].

The behaviour of an OWC does not depend solely on the sea state, but also on the damping exerted by the air turbine – represented in the model by the orifice – on the system [51]. In order to account for this effect when characterising the hydrodynamic response, a non-dimensional damping coefficient can be defined, following [47]:

$$B^* = \frac{\Delta p^{1/2}}{q} \frac{A_{OWC}}{\rho_a}, \tag{12}$$

where Δp is the relative pneumatic pressure, q represents air flowrate, ρ_a stands for air density and A_{OWC} is the horizontal surface area of the inner OWC chamber. Therefore, the values of the damping coefficients obtained for diameters of the orifice of d_o = 35, 42, 48 and 60 mm are B^* = 68.85, 50.50. 46.04 and 45.81, respectively.

3. Results

This section presents the results acquired during the experimental campaign and processed following the data analysis methods defined in Section 2.

3.1. Interaction with the wave field

The interaction between the wave field and the hybrid device is quantified using the reflection and transmission coefficients (K_R and K_T), obtained from the IRWA. Results for regular waves and for the four damping coefficients are represented versus the non-dimensional wave number (kh) in Figure 5. For random waves, results for the value of the damping coefficient corresponding to the orifice with area coefficient of 1% (B^* = 46.0) are plotted in Figure 6. In general, both (K_R and K_T) present a strong dependence on the wave period, and a weaker relationship with the damping exerted by the turbine.

For a certain wave height (Series C), the tendency of the K_R graph is clear: wave reflection decreases as the wave period increases (Figure 6). K_R increases, in general, with the non-dimensional wave number (kh). On the contrary, the transmission coefficient (K_T) increases with the wave period. In general, K_T values are around 0.32 for regular waves and 0.18 for random waves – with the exception

of the three smaller wave periods (T = 4, 5 and 6 s), where a decrease in wave transmission can be clearly observed when kh increases. In addition, an influence of the damping coefficient may be observed in both reflection and transmission, with the damping coefficient corresponding to the 1% orifice (B^* = 46.0) showing the largest effect – in particular for larger values of kh.

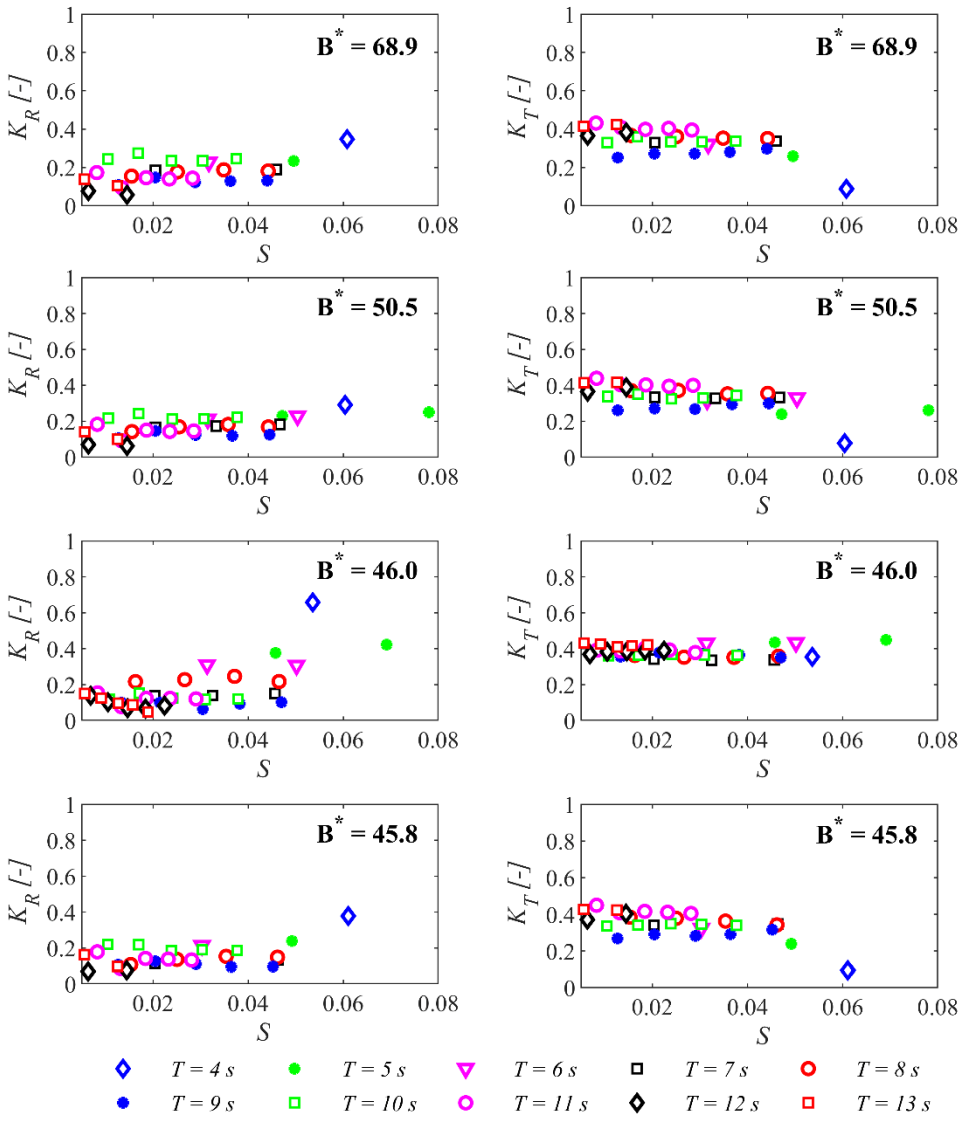

Figure 5: Values of K_R and K_T for different damping coefficients (B^*) and wave periods (T), regular waves (Series A); (data in prototype values)

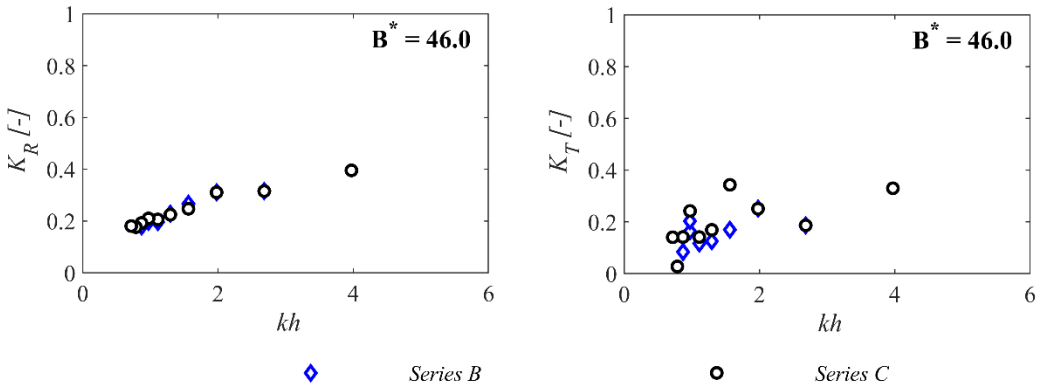

234

235 **Figure 6:** Values of K_R and K_T under random waves (Series B and C); (data in prototype values)

236 *3.2. Device performance*

237 The capture-width ratio (C_{WR}) was the tool for evaluating the performance of the WEC sub-system
238 (Equation 3). Figure 7 represents the C_{WR} versus the non-dimensional wave number (kh) for the four
239 damping coefficients tested and regular waves. The plot for random waves, Figure 8, considers the
240 damping coefficient value corresponding to the 1% orifice (B^* = 46.0). Furthermore, Figures 9 and 10
241 represent the capture-width ratio and power matrices respectively. Two peaks of maximum efficiency
242 can be clearly identified at different values of the wave period (T = 6 s and T = 9 s) – note that for the
243 peak occurring at the shortest wave period (T = 6 s), a significant amount of sloshing was observed at
244 the inner OWC chamber, during the experiments. It is clear that the main parameters influencing the
245 C_{WR} are the turbine damping and the wave period, followed by the non-dimensional wave number (kh).

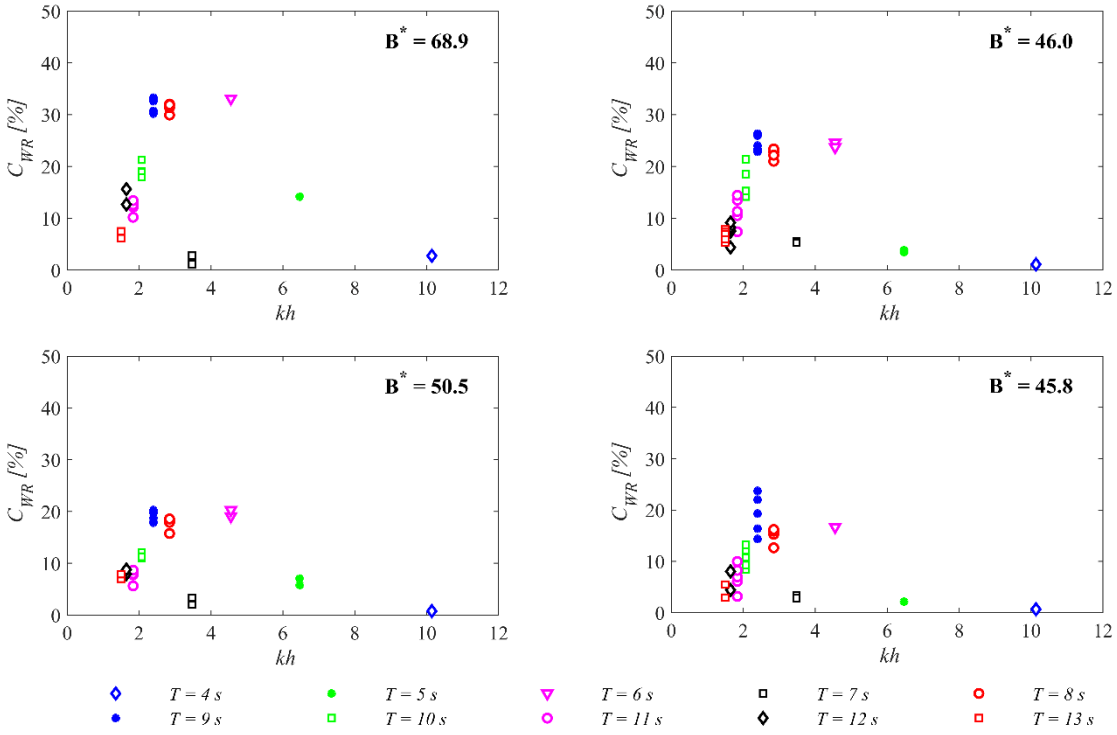

246

247 **Figure 7:** Capture width ratio (C_{WR}) for different damping coefficient (B^*) and wave period (T) values, and regular waves (Series A);
248 (data in prototype values)

249

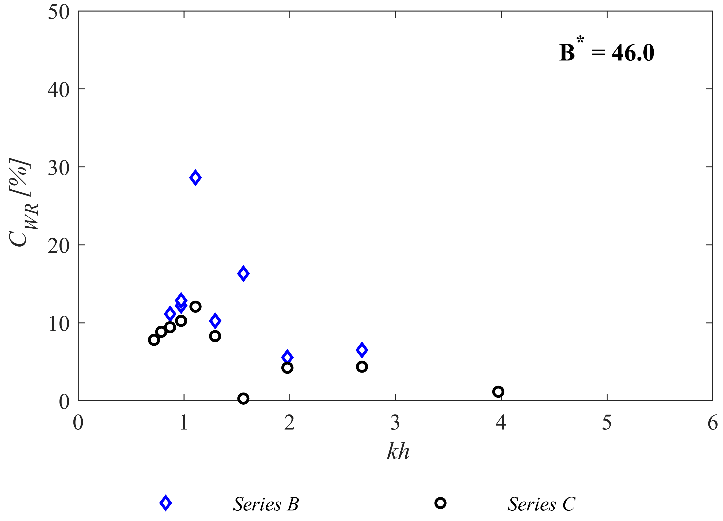

250

251 **Figure 8:** Capture width ratio (C_{WR}) and irregular waves (Series B and C); (data in prototype values)

252

253 Figures 7 and 8 show strong influence of the damping exerted by the turbine on the capture width ratio
254 (C_{WR}) – with average values of the C_{WR} 19%, 11%, 14% and 10% for turbine damping values of B^* =
255 68.9, 50.5, 46.0 and 45.8 respectively, for regular waves and 9% for irregular waves and B^* = 46.0.

The best performance is found for the 0.5% orifice sizes (B^*= 68.9) followed closely by the 1.0% (B^* = 46.0), while the worst performance can be seen at the 0.75% orifice (B^* = 50.5). The four orifices present maximum values of C_{WR} at (T = 6 s and T = 9 s) and minimum values of C_{WR} at (T = 7 s and T = 4 s). In addition, the C_{WR}, is strongly affected by the wave period, increasing this, in general, when the wave period decreases until it reaches its maximum value at T = 9 s, and then decreases to almost null values before finally increasing again for a second peak at T = 6 s. A similar behaviour can be also identified for irregular waves (Figure 8), in particular when fixing the significant wave height and varying the peak wave period (Series C).

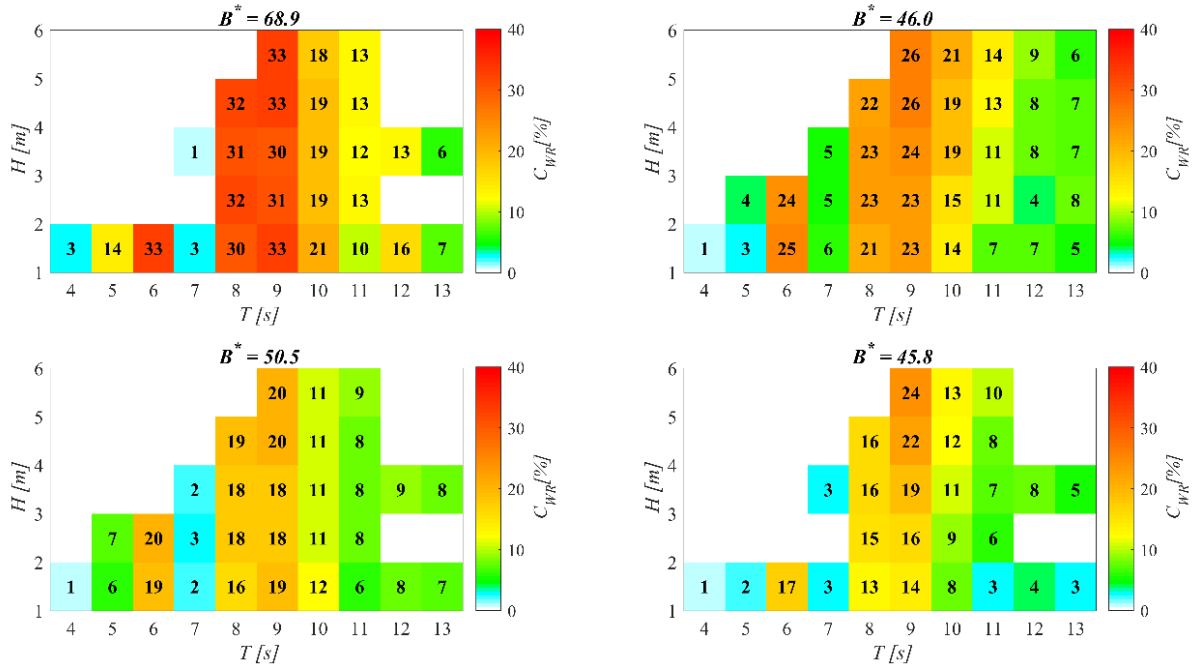

Figure 9: Matrices of the capture width ratio (C_{WR}) for different values of the damping coefficient (B^*) and regular waves (Series A), showing its variability in terms of the wave height (H) and wave period (T), (data in prototype values)

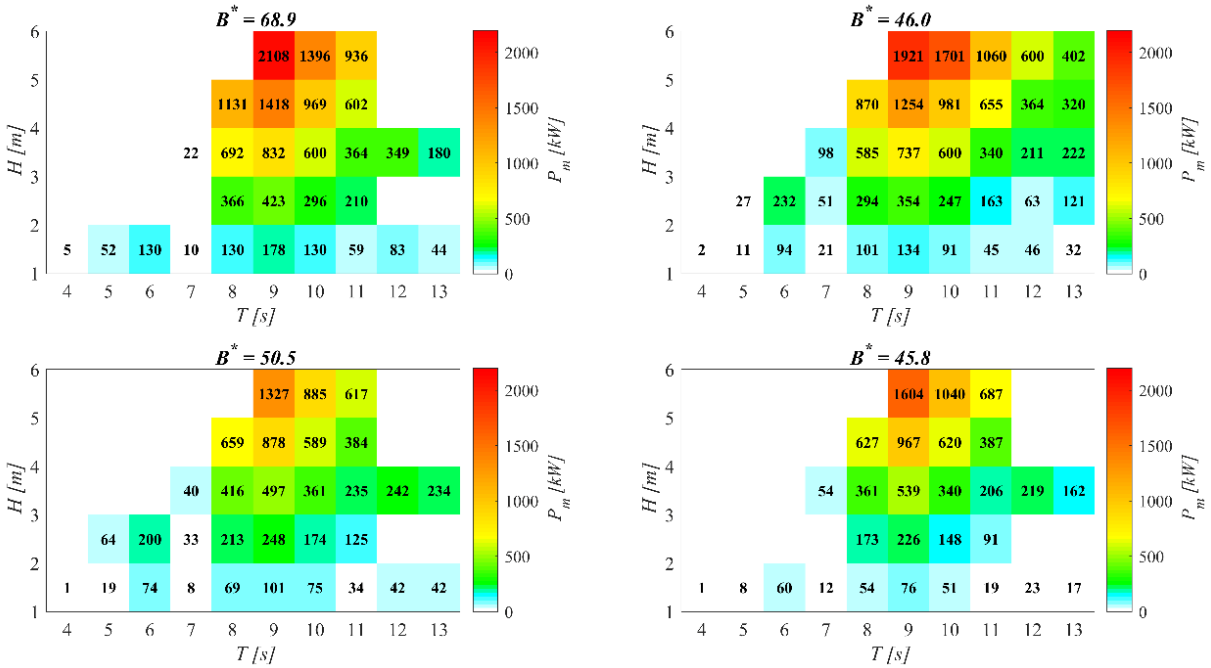

Figure 10: Matrices of the mean pneumatic power (P_m) for different values of the damping coefficient (B^*) and regular waves (Series A), showing its variability in terms of the wave height (H) and wave period (T), (data in prototype values)

To clarify the role of the different parameters influencing the performance of the converter, the matrices of capture-width ratio (C_{WR}) and average pneumatic power (P_m) are represented in terms of the wave height (H) and the wave period (T) and the four values of damping (B^*) for regular waves (Figures 9 and 10, respectively). Two regions of best performance appear in the capture-width ratio matrix (Figure 9), for the four damping values. The first corresponds to wave periods between T = 8 s and T = 11 s, with a primary peak at T = 9 s – note that for the 0.5% and 1.0% orifice sizes (B^* = 68.9 and B^* = 46.0) the extent of this area of best performance increases in comparison with the other two orifices, showing its maximum extent for the smallest orifice size (B^* = 68.9). The second is a narrow band concentrated at T = 6 s., which represents the secondary efficiency peak – note that for the smallest orifice size (B^* = 68.9) the width of this region extends to also T = 5 s. Furthermore, when analysing together the capture width and mean pneumatic matrices (Figures 9 and 10, respectively), the role of wave height on performance is apparent. Although this influence is less significant than that

284 exerted by wave period (T) or damping (B^*), it does have an effect, increasing the efficiency when
285 wave height increases.

286 *3.3. Device response*

287 The hybrid device response to the incident waves was analysed by means of the response amplitude
288 operator (RAO), which was used to characterise the response of the free surface in the chamber (RAO_C)
289 and the relative pressure (RAO_P). Figure 11 presents the results for regular waves and the values of the
290 damping coefficient versus the non-dimensional wave number (kh) and in Figure 12 versus the wave
291 frequency. It is clear that the main parameter influencing both RAOs is the turbine damping (B^*),
292 followed by the wave period (T), as seen in previous sections (Figure 11). In particular, RAO_P values
293 show a clear peak of maximum relative pneumatic pressure, around the area of best performance of
294 the hybrid device.

295 It is clear from Figure 11 that the damping coefficient (B^*) and the non-dimensional wave number (kh)
296 are the two parameters influencing the most the behaviour of both RAOs, showing RAO_C and RAO_P
297 opposite behaviours – i.e., when RAO_C increases RAO_P decreases and vice versa. Maximum values of
298 both RAOs are found for 0.5% and 1.0% orifice sizes ($B^* = 68.9$ and $B^* = 46.0$) – which is coherent
299 with the best performance data from previous section. Essentially, RAO_C tends to decrease when the
300 non-dimensional wave number (kh) increases along with the damping coefficient (B^*).

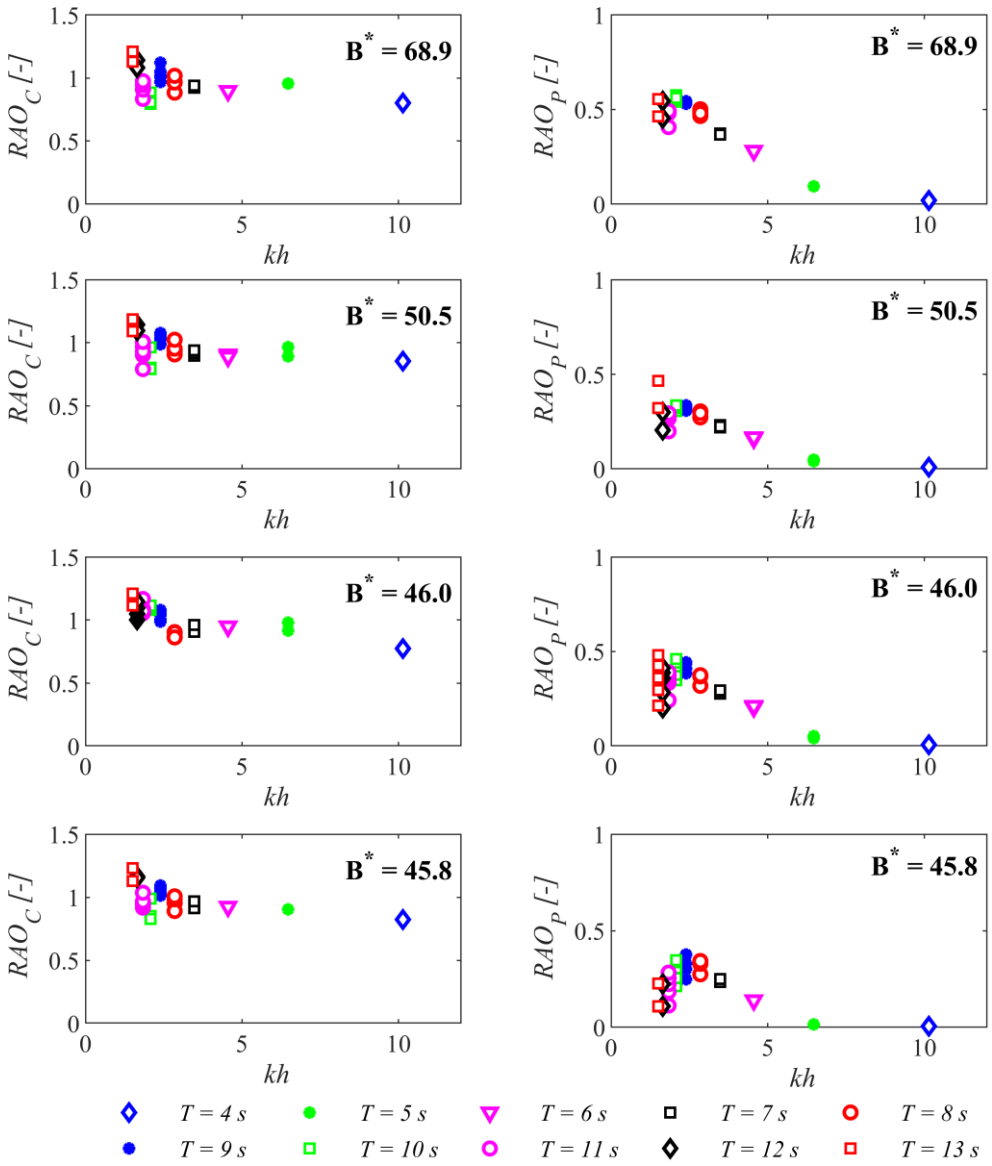

Figure 11: RAOC and RAOP versus non-dimensional wave number for various damping coefficients (B*) and wave periods (T) (Series A) (data in prototype values)

The conventional representation of the RAOs versus the wave frequency (f) is presented in Figure 12. It may be seen that the influence of the wave frequency on the values of RAO_C is accentuated for $f <$ 0.15 Hz. For higher frequencies, RAO_C tends to unity. The influence of the wave height on RAO_C is rather weak, and hardly noticeable for the lower wave frequencies. Furthermore, the turbine damping is the factor that primarily influences RAO_P, followed by wave frequency and, to a minor extent, wave height – whose relevance increases when the turbine damping decreases.

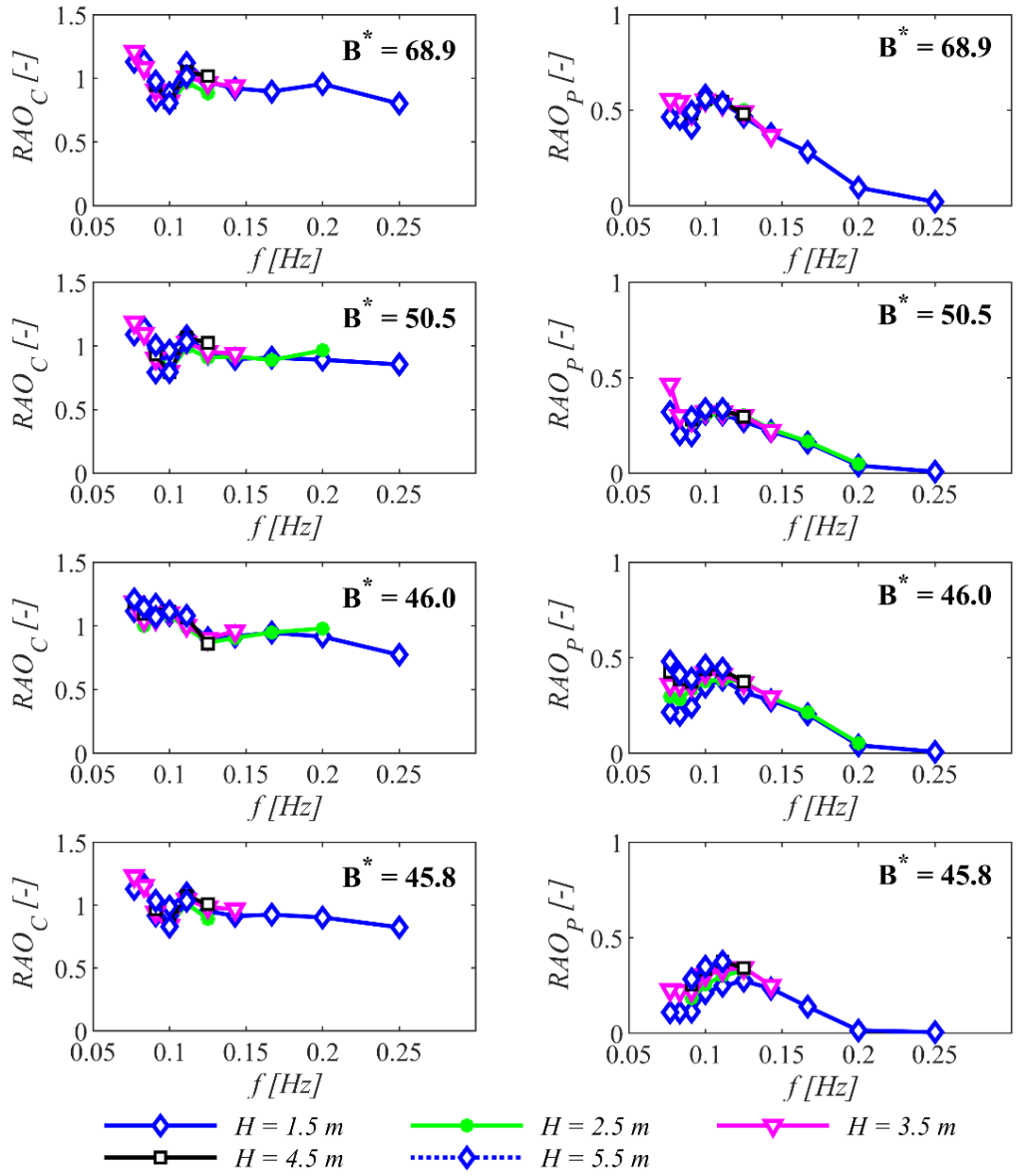

311

312 **Figure 12:** *RAO*$_C$ and *RAO*$_P$ versus wave frequency for various damping coefficients (B^*) and wave height (H)
313 (Series A) (data in prototype values)

314

315 *3.4. Run-up*

316 The study of the wave run-up at the front of the hybrid device, gives a valuable information for future
317 design and structural integration of the WEC sub-system into a monopile offshore wind substructure.
318 For this research the run-up was characterised by means of the run-up coefficient (C_R), for regular
319 waves, and the significant and maximum run-up coefficients (C_S and C_{max}, respectively) for irregular
320 waves. Figure 13 represents the C_R for regular waves and the four damping coefficients tested versus

the non-dimensional wave number (kh). Furthermore, C_S and C_{max} are represented for irregular waves in Figure 14 for the damping coefficient corresponding to the 1% orifice ($B^* = 46.0$) versus the non-dimensional wave number (kh). In general, the wave run-up is clearly controlled by the wave period, being the influence of the turbine damping less accentuated.

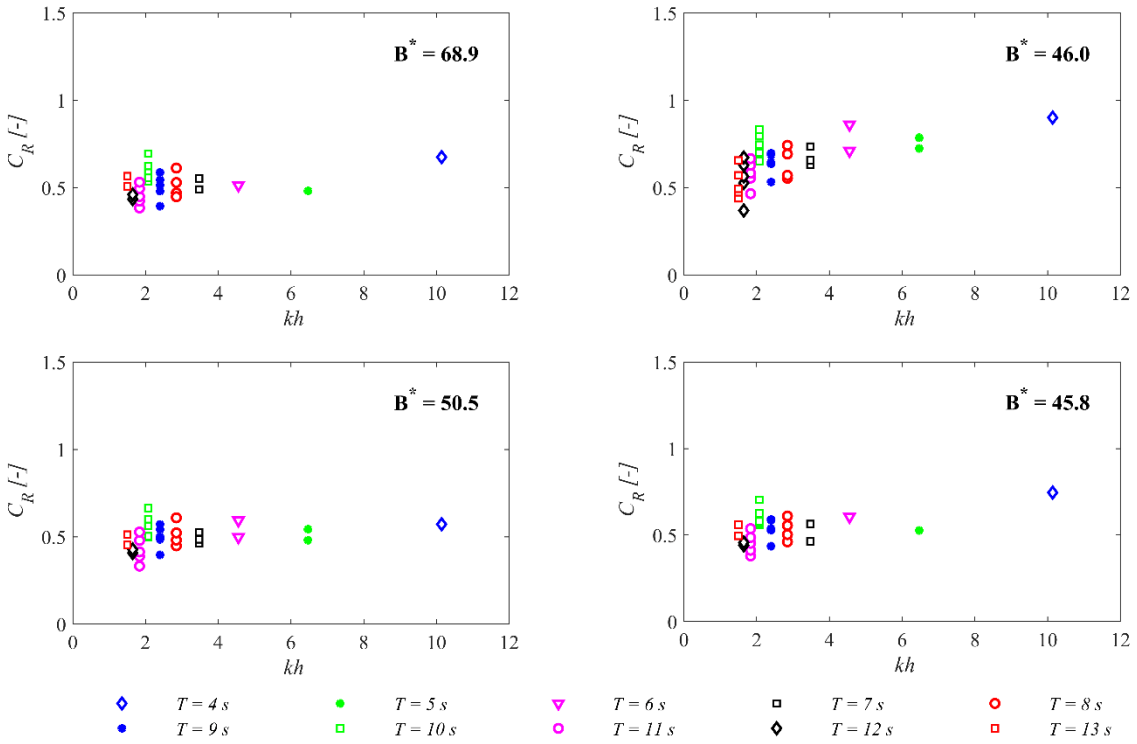

Figure 13: Run-up coefficient (C_R) for various damping coefficients (B^*) and wave periods (T) (Series A) (data in prototype values)

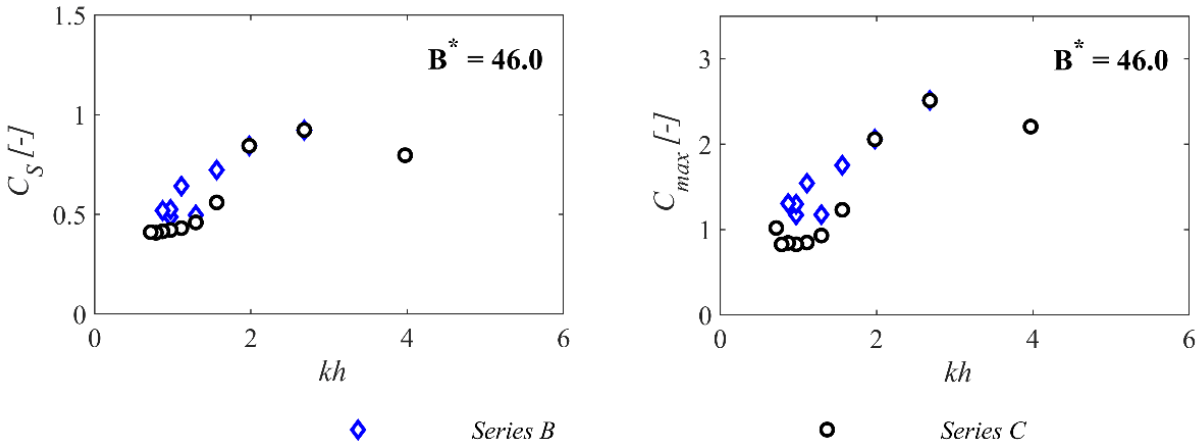

329

330 **Figure 14:** Significant and maximum run-up coefficients (CS and Cmax) under random waves (Series B and C)
331 (data in prototype values)

332

333 For regular waves (Figure 13), the run-up coefficient (C_R) shows, in general, values around 0.5. In
334 general, the wave run-up tends to increase when the wave period decreases, and shows two maxima,
335 for T = 10 s and T = 4 s. It is clear that the turbine damping value corresponding to the 1.0% orifice
336 size (B^* = 46.0) has the greatest influence on the run-up, leading, in general, to larger values. In
337 contrast, when looking at the run-up of irregular waves (Figure 14), the effect of the non-dimensional
338 wave number shows a clear influence on the wave run-up. This is testament of the strong influence of
339 the wave period, as may be observed from Series C data (where the significant wave height is kept
340 constant for a range of peak wave periods). Both significant and maximum run-up coefficients (C_S and
341 C_{max}, respectively), in most cases, increase considerably when the non-dimensional wave number
342 increases – when the peak wave period decreases. C_S ranges from about 0.5 to about 1, while C_{max}
343 varies from about 1 to over 2, with a maximum of C_{max} = 2.51 – i.e., a run-up that is two and a half
344 times larger than the incident wave.

345

4. Discussion

This work develops the University of Plymouth's hybrid wind-wave energy converter for installation on monopile offshore wind substructures. A comprehensive set of physical modelling tests were carried out to understand better its behaviour and further advance in the prototype development. A simplified model version of the hybrid device was defined and tested at 1:40 scale. Based on the results from these tests, the performance of the device and how this interacts with its surrounding wave field was studied to characterise its hydrodynamic response.

The wave height and period together with the damping exerted by the turbine were the parameters considered to investigate the hybrid device. A number of interchangeable orifice plates, with orifice sizes of different diameters, were used to model the turbine damping. A total of 184 tests, structured into four tests series, were performed considering regular and irregular waves. The hydrodynamic response of the hybrid device was fully characterised.

Concerning the interaction of the system with the wave field, the wave period was identified as the main parameter influencing the reflection and transmission coefficients – much more relevant than the turbine damping or wave height. K_R decreases when the wave period increases, a behaviour that is accentuated for irregular waves – note that this behaviour is coherent with that observed for previous versions of the hybrid device, as observed in [41], and other WECs (e.g., [52]). For regular waves, K_T, in general, increases with the wave period, while for irregular waves a more random behaviour is observed, and further investigation is needed to determine a clear pattern; however, most K_T values for irregular waves are grouped around 0.18. A reflection of between 5% and 66% of the incident wave power and a transmission of between 3% and 45% was observed. These values help understand the implications that the 'shadow effect' may have at a larger scale – at the wind farm scale or on the leeward coasts.

When looking at the device performance, the damping exerted by the turbine and the wave period stand out as the main factors determining the capture-width ratio. The influence on the selection a turbine that exerts the optimum damping OWC chamber highlights the importance of an optimum coupling between turbine and chamber during the design phase, as previously identified by several authors (e.g., [53]). Moreover, the wave period plays a significant role in the device performance; two resonant peaks were identified T = 9 s and T = 6 s). The first peak is linked to the resonance of the free surface motion in heave and the chamber itself, as is well known, in the literature (e.g., [54]). By contrast, the peak observed at the shorter wave period (T = 6 s) is linked to a resonance effect induced by the sloshing of the inner free surface, and this sloshing was observed visually through the clear acrylic lid of the model at this frequency. Further research is needed to fully understand this effect; however, the authors believe that it may well be induced by the interaction between the diffracted waves from to the inner monopile and the OWC chamber. For the wave conditions and damping values considered in this research, the highest damping coefficient (B^* = 68.9) – i.e., the smallest orifice diameter size – generally, results in the highest values of the capture-width ratio. The capture-width ratio matrix shows two areas of maximum efficiency, which match the two resonant peaks across most of the wave heights.

From the analysis of the response of the free surface oscillation inside the chamber (RAO_C) and the relative pneumatic pressure in the chamber (RAO_P) – i.e., the two fundamental elements affecting the power output of an OWC – it is clear that both RAOs are mostly influenced by the turbine damping and wave period, not least RAO_P – when the damping coefficient increases, RAO_C decreases and RAO_P increases. The maximum values of both RAOs are achieved simultaneously by turbine damping values corresponding to orifice apertures of 0.5% and 1.0% (B^* = 68.9 and 46.0, respectively), which explains the better performance shown by these turbine damping values. In general, RAO_C increases when the wave period increases, while RAO_P shows a maximum for wave periods between T = 8 s and T = 10 s

and decreases for the remaining periods. It should be noted that this region of increased pressure matches the area of best performance of the hybrid device observed in the C_{WR} matrix (Figure 9).

Finally, the study of the run-up at the front of the model, by means of the run-up coefficient, shows a strong influence of the wave period on the wave run-up, which increases as the wave period decreases. An influence of the turbine damping over the run-up can also be observed, with the turbine damping corresponding to the 1.0% orifice size ($B^* = 46.0$) leading to the largest run-up values. Furthermore, for regular waves the run-up ranges between 33% and 90% of the incident wave height. For irregular waves, while the significant run-up ranges between 41% and 92% of the incident wave height, similar values to those observed for regular waves the maximum run-up ranges between 83% and 251% of the incident wave height.

5. Conclusions

In this work, the University of Plymouth's hybrid wind-wave energy converter was further developed for installation in monopile substructures and thoroughly investigated through physical modelling. On the basis of the results from the experimental campaign, two main outcomes were obtained. First, the proposed hybrid system was successfully proved as valid concept to be considered for monopile substructures – the most common type of substructures for offshore wind turbines. Then, the hydrodynamic response of the WEC sub-system (OWC) was fully characterised, This lead to a better understanding not only in the relationship between OWC performance, the incident wave field and the turbine damping, but also in the interaction between device and the wave field itself.

Based on the analysis of the hydrodynamic response of the hybrid device, the following main conclusions may be drawn:

- The hybrid device interacts with the near wave field by reflecting between 5% and 66% of the incident wave power and transmitting between 3% and 45%.

- The best performance occurs with the turbine damping corresponding to the 0.5% orifice, followed closely by the 1.0% orifice.
- Two resonant peaks of best performance are found at T = 9 s and T = 6 s.
- A wider area of best performance is found between T = 8 s and T = 11 s.
- The RAO was used to understand the effect of the incident wave field on the two main parameters influencing the device power output – the relative pneumatic pressure between the chamber and the atmosphere, and the free surface oscillation inside the chamber.
- The RAO of free surface oscillation in the OWC chamber increases when the wave period increases.
- The relative pneumatic pressure between inside the OWC chamber and the atmosphere shows a peak of maximum RAO_P for wave periods between T = 8 s and T = 10 s, matching the area of best performance observed in the capture with matrix.
- The wave run-up is strongly influenced by the wave period; furthermore, the run-up of irregular waves being between 1 and 2 times larger than that of regular waves.

In sum, the wind-wave energy converter developed in this work represents a viable hybrid solution for integration with existing offshore wind turbines with a monopile substructure. This work contributes to understanding the interaction between the hybrid device and the near wave field, which is relevant in assessing the impact of this type of devices on the marine environment. Further work is required to develop this hybrid system, notably to ascertain the structural implications of the WEC sub-system on the substructure.

Supplementary Materials

The research materials supporting this publication may be accessed at [link to the enclosed dataset will be added here in the final version of the manuscript after acceptance by the editorial team]. If

you have any question regarding these research materials, please contact the corresponding author of this paper.

Acknowledgements

This work was carried out with the financial support of the School of Engineering of the University of Plymouth. The Authors are grateful to the Horns Rev 3 wind farm and the Danish national grid operator (Energinet) for the resource data of the site. In addition, the Authors are also grateful to Mr Miles Newton, Mr Harry Ross and the COAST Lab technical support staff for their help during the experimental campaign.

Author Contributions:

All the authors conceived and designed the physical modelling; Carlos Perez-Collazo conducted the experimental campaign, analysed the data and wrote the paper; Richard Pemberton, Deborah Greaves and Gregorio Iglesias gave helpful comments and revised the paper; and all the authors have reviewed and approved this manuscript.

Appendix A

Two statistical operators, the correlation coefficient (R^2) and the normalised root mean square error (*NRMSE*), are defined to evaluate results from the repeatability test Series RA and RB.

$$R^2 = \frac{\left(\sum_{i=1}^{N}(x_i-\bar{x})(y_i-\bar{y})\right)^2}{\sum_{i=1}^{N}(x_i-\bar{x})\sum_{i=1}^{N}(y_i-\bar{y})}, \quad (20)$$

where x_i and y_i are the equivalent data points from the two different data sets, of length N; and $\bar{x}$ and $\bar{y}$ are their respective arithmetic averages. This coefficient evaluates the relationship between two variables, giving an idea on how similar are the time series compared, being 1 when both series are identical.

$$NRMSE = \frac{1}{x_{max}-x_{min}}\sqrt{\frac{1}{N}\sum_{i=1}^{N}(x_i-y_i)^2}, \quad (21)$$

where x_{max} and x_{min} are the maximum and the minimum values of the data set used as reference.

460 **Figure captions**

461 **Figure 1:** University of Plymouth's hybrid wind-wave energy converter: (a) conceptual
462 representation of the hybrid system for monopile offshore wind substructures; and (b) perspective
463 view of the WEC sub-system; (partially reproduced from [47]).
464 **Figure 2**: 1:40 scale model of the hybrid device: (a) being tested at the University of Plymouth's
465 COAST Laboratory and (b) a sketch showing front and side views of the model.
466 **Figure 3**: Horns Rev 3 significant wave height – energy period scatter diagram. The curves represent
467 wave power isolines, and the numbers, hours in an average year of the corresponding energy bin.
468 **Figure 4**: Lateral view of the flume and schematic of the wave gauge layout.
469 **Figure 5:** Values of K_R and K_T for different damping coefficients (B^*) and wave periods (T), regular
470 waves (Series A); (data in prototype values).
471 **Figure 6:** Values of K_R and K_T under random waves (Series B and C); (data in prototype values).
472 **Figure 7:** Capture width ratio (C_{WR}) for different damping coefficient (B^*) and wave period (T)
473 values, and regular waves (Series A); (data in prototype values).
474 **Figure 8:** Capture width ratio (C_{WR}) and irregular waves (Series B and C); (data in prototype values).
475 **Figure 9:** Matrices of the capture width ratio (C_{WR}) for different values of the damping coefficient
476 (B^*) and regular waves (Series A), showing its variability in terms of the wave height (H) and wave
477 period (T), (data in prototype values).
478 **Figure 10:** Matrices of the mean pneumatic power (Pm) for different values of the damping
479 coefficient (B^*) and regular waves (Series A), showing its variability in terms of the wave height (H)
480 and wave period (T), (data in prototype values).
481 **Figure 11:** RAO_C and RAO_P versus non-dimensional wave number for various damping coefficients
482 (B^*) and wave periods (T) (Series A) (data in prototype values).
483 **Figure 12:** RAO_C and RAO_P versus wave frequency for various damping coefficients (B^*) and wave
484 height (H) (Series A) (data in prototype values).

Figure 13: Run-up coefficient (C_R) for various damping coefficients (B^*) and wave periods (T) (Series A) (data in prototype values).

Figure 13: Significant and maximum run-up coefficients (C_S and C_{max}) under random waves (Series B and C) (data in prototype values).

Table captions

Table 1: Model characteristics and dimensions.

Table 2: Position of wave gauges and model.

Table 3: Wave conditions for Series A, regular waves (data in prototype values)

Table 4: Wave conditions for Series B and C, irregular waves (data in prototype values)

Table 5: Average values of R^2 (correlation coeff.) and *NRMSE* (normalised root-mean-square error) for the repeatability tests series

References

[1] Weisse R, von Storch H, Callies U, Chrastansky A, Feser F, Grabemann I, et al. Regional Meteorological–Marine Reanalyses and Climate Change Projections. Bulletin of the American Meteorological Society 2009;90:849–60. doi:10.1175/2008bams2713.1.

[2] Azzellino A, Conley D, Vicinanza D, Kofoed JP. Marine Renewable Energies: Perspectives and Implications for Marine Ecosystems. The Scientific World Journal 2013;2013. doi:10.1155/2013/547563.

[3] Astariz S, Iglesias G. Wave energy vs. other energy sources: A reassessment of the economics. International Journal of Green Energy 2016;13:747–55. doi:10.1080/15435075.2014.963587.

[4] GWEC,. Global Wind 2017. Global Wind Energy Council (GWEC); 2018.

[5] Remy T, Mbistrova A. Offshore Wind in Europe: Key trends and statistics 2017. Brussels, Belgium: Wind Europe; 2018.

[6] Jeffrey H, Sedgwick J. ORECCA. European Offshore Renewable Energy roadmap. 2011.

[7] Dalton G, Bardócz T, Blanch M, Campbell D, Johnson K, Lawrence G, et al. Feasibility of investment in Blue Growth multiple-use of space and multi-use platform projects; results of a novel assessment approach and case studies. Renewable and Sustainable Energy Reviews 2019;107:338–59. doi:10.1016/j.rser.2019.01.060.

[8] van den Burg S, Stuiver M, Norrman J, Garção R, Söderqvist T, Röckmann C, et al. Participatory Design of Multi-Use Platforms at Sea. Sustainability 2016;8:127. doi:10.3390/su8020127.

[9] Astariz S, Perez-Collazo C, Abanades J, Iglesias G. Co-located wind-wave farm synergies (Operation & Maintenance): A case study. Energy Conversion and Management 2015;91:63–75. doi:10.1016/j.enconman.2014.11.060.

[10] Quevedo E, Delory M, Castro A, Llinas O, de Lara J, Papandroulakis N, et al. Multi-use offshore platform configurations in the scope of the FP7 TROPOS Project, 2013, p. 1–7.

[11] Stuiver M, Soma K, Koundouri P, van den Burg S, Gerritsen A, Harkamp T, et al. The Governance of Multi-Use Platforms at Sea for Energy Production and Aquaculture: Challenges for Policy Makers in European Seas. Sustainability 2016;8:333. doi:10.3390/su8040333.

[12] Perez-Collazo C, Greaves D, Iglesias G. A review of combined wave and offshore wind energy. Renewable & Sustainable Energy Reviews 2015;42:141–53. doi:10.1016/j.rser.2014.09.032.

[13] Perez-Collazo C, Jakobsen MM, Buckland H, Fernandez Chozas J. Synergies for a wave-wind energy concept, EWEA; 2013, p. 1–10. doi:10.13140/2.1.5155.1523.

[14] Casale C, Serri L, Stolk N, Yildiz I, Cantù M. Synergies, innovative designs and concepts for multipurpose use of conversion platforms. Results of ORECCA Project - WP4. Munchen, Germany: ORECCA; 2012.

[15] Astariz S, Abanades J, Perez-Collazo C, Iglesias G. Improving wind farm accessibility for operation & maintenance through a co-located wave farm: Influence of layout and wave climate. Energy Conversion and Management 2015;95:229–41. doi:10.1016/j.enconman.2015.02.040.

[16] CORDIS. MARINA Platform 2017.

[17] CORDIS. ORECCA 2019.

[18] CORDIS. TROPOS 2019.

[19] CORDIS. H2OCEAN 2017.

[20] CORDIS. MERMAID 2017.

[21] Floating Power Plant AS. Poseidon Floating Power web page 2018.

[22] NEMOS GmBH. NEMOS web page 2019.

[23] Wave Star AS. Wave Star Energy web page 2012.

[24] Legaz MJ, Coronil D, Mayorga P, Fernández J. Study of a hybrid renewable energy platform: W2Power. Proceedings of the International Conference on Offshore Mechanics and Arctic Engineering - OMAE, vol. 11A, 2018. doi:10.1115/OMAE2018-77690.
[25] Zanuttigh B, Angelelli E, Kortenhaus A, Koca K, Krontira Y, Koundouri P. A methodology for multi-criteria design of multi-use offshore platforms for marine renewable energy harvesting. Renewable Energy 2016;85:1271–89. doi:10.1016/j.renene.2015.07.080.
[26] O'Sullivan K. Feasibility of compbined wind-wave energy platform. PhD. University College Cork, 2014.
[27] Hanssen JE, Margheritini L, O'Sullivan K, Mayorga P, Martinez I, Arriaga A, et al. Design and performance validation of a hybrid offshore renewable energy platform, 2015, p. 1–8. doi:10.1109/EVER.2015.7113017.
[28] O'Sullivan K, Murphy J. Deterministic Economic Model for Wind-Wave Energy Hybrid Energy Conversion Systems, 2012, p. 7.
[29] Sarmiento J, Iturrioz A, Ayllón V, Guanche R, Losada IJ. Experimental modelling of a multi-use floating platform for wave and wind energy harvesting. Ocean Engineering 2019;173:761–73. doi:https://doi.org/10.1016/j.oceaneng.2018.12.046.
[30] Veigas M, Iglesias G. A Hybrid Wave-Wind Offshore Farm for an Island. International Journal of Green Energy 2015;12:570–6. doi:10.1080/15435075.2013.871724.
[31] Weiss CVC, Guanche R, Ondiviela B, Castellanos OF, Juanes J. Marine renewable energy potential: A global perspective for offshore wind and wave exploitation. Energy Conversion and Management 2018;177:43–54. doi:https://doi.org/10.1016/j.enconman.2018.09.059.
[32] Fusco F, Nolan G, Ringwood JV. Variability reduction through optimal combination of wind/wave resources – An Irish case study. Energy 2010;35:314–25. doi:10.1016/j.energy.2009.09.023.
[33] Astariz S, Iglesias G. Selecting optimum locations for co-located wave and wind energy farms. Part I: The Co-Location Feasibility index. Energy Conversion and Management 2016;122:589–98. doi:10.1016/j.enconman.2016.05.079.
[34] Stoutenburg ED, Jenkins N, Jacobson MZ. Power output variations of co-located offshore wind turbines and wave energy converters in California. Renewable Energy 2010;35:2781–91. doi:10.1016/j.renene.2010.04.033.
[35] Li W, Shen-Ron J, Chao-Nan L, Hao-Wen L, Yi-Hsuan H, Yi-Ting C. Analysis of an integrated offshore wind farm and seashore wave farm fed to a power grid through a variable frequency transformer, 2011, p. 1–7. doi:10.1109/pes.2011.6039072.
[36] Astariz S, Iglesias G. Output power smoothing and reduced downtime period by combined wind and wave energy farms. Energy 2016;97:69–81. doi:10.1016/j.energy.2015.12.108.
[37] Astariz S, Iglesias G. Enhancing Wave Energy Competitiveness through Co-Located Wind and Wave Energy Farms. A Review on the Shadow Effect. Energies 2015;8:7344. doi:10.3390/en8077344.
[38] Astariz S, Perez-Collazo C, Abanades J, Iglesias G. Towards the optimal design of a co-located wind wave farm. Energy 2015;84:15–24. doi:10.1016/j.energy.2015.01.114.
[39] Perez-Collazo C, Greaves D, Iglesias G. Proof of concept of a novel hybrid wind-wave energy converter, 2018, p. 1–11. doi:0.1115/OMAE2018-78150.
[40] Perez-Collazo C, Greaves D, Iglesias G. A Novel Hybrid Wind-Wave Energy Converter for Jacket-Frame Substructures. Energies 2018;11:637. doi:10.3390/en11030637.
[41] Perez-Collazo C, Greaves D, Iglesias G. Hydrodynamic response of the WEC sub-system of a novel hybrid wind-wave energy converter. Energy Conversion and Management 2018;171:307–25. doi:https://doi.org/10.1016/j.enconman.2018.05.090.
[42] Chakrabarti SK. Offshore structure modeling. vol. 9. Singapore: World Scientific; 1994.
[43] Hann M, Perez-Collazo C. Chapter 7: Physical Modelling. In: Greaves D, Iglesias G, editors. Wave and Tidal Energy, West Sussex, UK: John Wiley & Sons Ltd; 2018, p. 233–88.

[44] López I, Carballo R, Iglesias G. Site-specific wave energy conversion performance of an oscillating water column device. Energy Conversion and Management 2019;195:457–65. doi:https://doi.org/10.1016/j.enconman.2019.05.030.
[45] Sheng W, Lewis A, Alcorn R. On wave energy extraction of oscillating water column device, 2012.
[46] Energinet. dk. Horns Rev 3 Offshore Wind Farm: Metocean. Energinet.dk; 2014.
[47] López I, Pereiras B, Castro F, Iglesias G. Performance of OWC wave energy converters: influence of turbine damping and tidal variability. International Journal of Energy Research 2015;39:472–83. doi:10.1002/er.3239.
[48] Collazo CP, Rodriguez JGI, Greaves D, University of Plymouth. Wave energy capture device. WO2016185189 A1, 2015.
[49] Mansard EP, Funke ER. The measurement of incident and reflected spectra using a least squares method. vol. 1, 1980.
[50] Baquerizo A, Losada MA, Smith JM. Wave reflection from beaches: A predictive model. Journal of Coastal Research 1998:291–8.
[51] Pereiras B, López I, Castro F, Iglesias G. Non-dimensional analysis for matching an impulse turbine to an OWC (oscillating water column) with an optimum energy transfer. Energy 2015;87:481–9. doi:10.1016/j.energy.2015.05.018.
[52] Zanuttigh B, Angelelli E, Kofoed JP. Effects of mooring systems on the performance of a wave activated body energy converter. Renewable Energy 2013;57:422–31. doi:10.1016/j.renene.2013.02.006.
[53] Simonetti I, Cappietti L, Elsafti H, Oumeraci H. Optimization of the geometry and the turbine induced damping for fixed detached and asymmetric OWC devices: A numerical study. Energy 2017;139:1197–209. doi:10.1016/j.energy.2017.08.033.
[54] He F, Zhang H, Zhao J, Zheng S, Iglesias G. Hydrodynamic performance of a pile-supported OWC breakwater: An analytical study. Applied Ocean Research 2019. doi:https://doi.org/10.1016/j.apor.2019.03.022.